Generalized Synthetic Strategy for Transition Metal Doped Brookite-Phase TiO_2 Nanorods

Zhiyong Zhang[1,#], Qiyuan Wu[2,#], Grayson Johnson[1,#], Yifan Ye[3], Xing Li[4], Na Li[4], Meiyang Cui[1], Jennifer D. Lee[5], Chang Liu[1], Shen Zhao[4], Shuang Li[4], Alexander Orlov[2], Christopher B. Murray[5], Xu Zhang[6], T. Brent Gunnoe[1], Dong Su[4,*], Sen Zhang[1,*]

[1]Department of Chemistry, University of Virginia, Charlottesville, Virginia 22904, USA;
[2]Department of Materials Science and Chemical Engineering, State University of New York, Stony Brook, New York 11794, USA;
[3]Advanced Light Source, Lawrence Berkeley National Laboratory, Berkeley, California 94720, USA;
[4]Center for Functional Nanomaterials, Brookhaven National Laboratory, Upton, New York 11973, USA;
[5]Department of Chemistry, University of Pennsylvania, Philadelphia, Pennsylvania 19104, USA;
[6]Department of Physics and Astronomy, California State University Northridge, Northridge, California 91330, USA.

Abstract We report a generalized wet-chemical methodology for the synthesis of transition metal (M) doped brookite-phase TiO_2 nanorods (NRs) with unprecedented wide-range tunability in dopant composition (M = V, Cr, Mn, Fe, Co, Ni, Cu, Mo, etc.). These quadrangular NRs can selectively expose {210} surface facets, which is induced by their strong affinity for oleylamine stabilizer. This structure is well preserved with variable dopant compositions and concentrations, leading to a diverse library of TiO_2 NRs wherein the dopants in single-atom form are homogeneously distributed in a brookite-phase solid lattice. This synthetic method allows tuning of dopant-dependent properties of TiO_2 nanomaterials for new opportunities in catalysis applications.

Central to functional nanomaterials is the ability to synthetically control nanocrystals physical dimensions, compositions, and structures with atomic scale precision.[1-7] TiO_2 is one of the most studied metal oxides nanomaterials[8-15] due to its unique semiconducting and oxygen carrying properties and important applications in optoelectronics,[16] batteries,[17-19] heterogeneous catalysis[20, 21] and photocatalysis.[22-25] For example, TiO_2 can provide active lattice oxygen species and strong interactions with metal nanoparticles, allowing the modulation of kinetics for many heterogeneous catalytic reactions.[26-28] TiO_2 can also absorb photons to generate excited electrons and holes, driving redox reactions for photocatalytic water splitting and photo-reforming processes.[29-32] To maximize the benefits of these applications, an emerging aspect in the studies of TiO_2 nanostructures is to dope them with foreign elements, including cations (e.g., Fe, Sn)[33, 34] or/and anions (e.g., C, N, F).[35-39] which can tune lattice oxygen activity as well as improve TiO_2's electronic structure, surface acidity/basicity, and photon absorption, enabling the enhanced catalytic properties.[40-42]

Such a doping strategy has been extensively studied for the rutile- and anatase-phase TiO_2 nanomaterials.[33-36, 41] In contrast, brookite TiO_2, another polymorph of TiO_2, is rarely studied due to the challenge of synthesizing the pure brookite phase. Recently, a high-yield synthesis of brookite-phase TiO_2 nanorods (NRs) has been reported via the hydrolysis of titanium chloride precursor,[14] which promoted electron-hole separation under solar irradiation due to the one-dimensional (1-D) structure and therefore delivered a record-high photocatalytic activity towards photo-reforming of ethanol/glycerol for hydrogen (H_2) production.[43] This success for the synthesis of brookite-phase TiO_2 NRs leads to the present work exploring a robust approach to doping for further enhanced catalytic properties. We found that single, dual, or multiple transition metal (M) dopants in a broad range (M = V, Cr, Mn, Fe, Co, Ni, Cu, Mo, etc., as illustrated in **Figure 1**) can be homogeneously doped into monodisperse single-crystalline brookite-phase TiO_2 NRs (M-TiO_2). The resultant M-TiO_2 NRs showed consistencies in physical dimensions and surface facets, thereby creating a new class of well-defined TiO_2 nanocrystals with tunable compositions as well as optical and catalytic properties. Using Fe-TiO_2 NRs as a model system, we demonstrated that controlling Fe-dopant level substantially enhances the photocatalytic performance of TiO_2 brookite-phase nanomaterials.

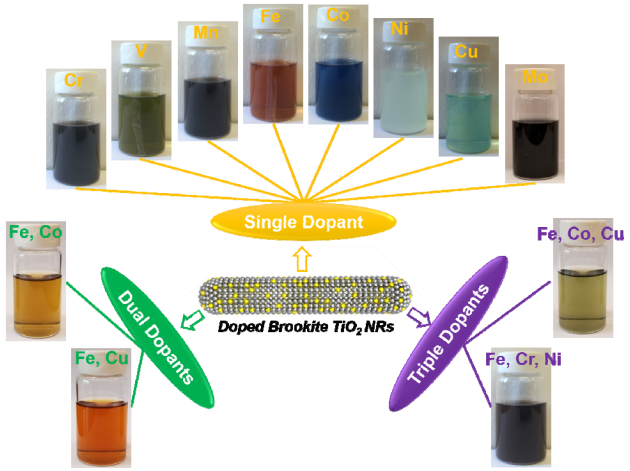

Figure 1. Diverse M-TiO_2 brookite-phase NRs synthesized by the reported synthetic methodology.

The M-TiO_2 NRs were synthesized via an organic solution colloidal hydrolysis method {see the Supporting Information (SI)}. Typically, $TiCl_4$ precursor dissolved in oleic acid (OAc) is decomposed in a mixture of 1-octadecene (ODE) and oleylamine (OAm). At high temperature (290 °C), OAm and OAc can react to generate a small amount of water, resulting in slow hydrolysis and condensation of $TiCl_4$ along with the release of HCl. Unlike the previous method,[43, 44] we incorporated M-oleate precursor in our synthesis by mixing it with $TiCl_4$-OAc to produce M-TiO_2. It is known that M-oleate, such as Fe-oleate, can be rapidly decomposed to initiate metal oxide nucleation only at temperatures higher than 310 °C. [45] Our reaction temperature (290 °C) and the presence of HCl minimize the possibility of MO_x formation. As a result, M is doped into the TiO_2 matrix, producing M-TiO_2 that can be well-dispersed in non-polar solvent and exhibit distinct colors relative to undoped TiO_2. As summarized in **Figure 1**, this strategy can be generalized to all first-row transition metal dopants and even second-row metals (e.g., Mo) as well as binary and ternary combinations.

Transmission electron microscopy (TEM) and scanning TEM (STEM) images show that the as-synthesized mono-M-TiO_2 (**Fig-**

ure 2A, **S1B-G**, and **S2A**), bi-M-TiO_2 (**Figure S3**), tri-M-TiO_2 (**Figure S4**), and pristine TiO_2 (**Figure S1A** and **S2B**) samples have a consistent NR morphology with an average width of 4.2 ± 0.5 nm and a length of 30-50 nm. These M-TiO_2 NRs preserve the brookite phase, as indicated by their powder X-ray diffraction (XRD) patterns (JCPDS No. 29-1360, orthorhombic) with the characteristic brookite (121) peak at 2θ = 30.81° (**Figure S5**). By adjusting the precursor M/Ti molar ratio, the M dopant level can be controlled (see SI). TEM images in **Figure 2A** and **S1H** confirm the Fe atomic concentration can be increased up to 10% (out of all cations Fe + Ti, obtained with energy-dispersive X-ray spectroscopy (EDS)) without any obvious morphology change. But we noticed that higher concentrations of M-oleate precursor do not result in further increased doping level. Instead, M remains in the solution, probably because the stability of brookite-phase TiO_2 lattice does not favor the incorporation of a high-concentration of dopants.

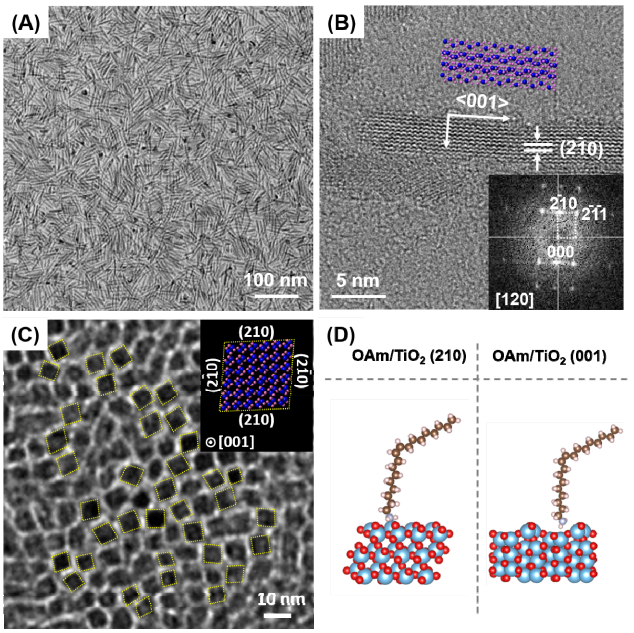

Figure 2. (**A**) TEM and (**B**) HRTEM images of the as-synthesized Fe-TiO_2 (10% Fe); (**C**) TEM image of vertically aligned Fe-TiO_2 (10% Fe) assembly; (**D**) Optimized OAm adsorption on brookite-phase TiO_2 (210) and (001) planes. Insets in **B** and **C** illustrate the corresponding TiO_2 atomic models with purple and pink atoms being Ti and O. In the DFT models, the color scheme is red (O), grey (C), white (H), blue (N), and teal (Ti).

High-resolution TEM (HRTEM) images of the representative Fe-TiO_2 (**Figure 2B**) and pristine TiO_2 NRs (**Figure S6**) suggest these NRs are single crystalline and grow along the <001> direction. Fast Fourier transform of HRTEM images in **Figure 2B** indicates that the side facets might be {210} planes. Thanks to their monodisperse size and morphology, the TiO_2 and Fe-TiO_2 NRs can be easily aligned into ordered assemblies at the interface of air/diethylene glycol via the previous method (SI, **Scheme S1**).[46] The TEM images (**Figure 2C** and **S7**) viewed along the NR longitudinal direction, based on their vertical assemblies, show a rhombic NR cross-section shape with an angle of ~80°/100°, confirming that the NRs expose four {210} planes as the side facets.

Density functional theory (DFT) calculations (SI) were performed to evaluate the binding between surfactants/ions (OAm, OAc, and Cl^-) and two TiO_2 facets (001) and (210) to understand the formation mechanism of quadrangular NRs (**Figure 2D**). We found, in agreement with Gong *et al.*,[47] that the (001) plane of brookite-phase TiO_2 is not stable and undergoes a 1x1 reconstruction both under vacuum and in the presence of surfactant (**Figure S8**). Moreover, the adsorption energies (E_{ad}) of OAm, OAc and Cl^- on the (210) plane were calculated to be -0.93 eV, -0.44 eV and -0.72 eV, all stronger compared to those on the (001) plane (-0.07 eV, -0.24 eV and -0.06 eV, respectively) (**Table S1**). As a result, (210) planes can be preferentially exhibited because of the stronger binding with the surfactants/ions, and such a structure is preserved when only a low concentration of dopant is incorporated. It is worth noting that OAm is present in a much larger amount than OAc and Cl^- in our synthesis and therefore played the most important role in stabilizing (210) plane due to the strongest E_{ad} (-0.93 eV).

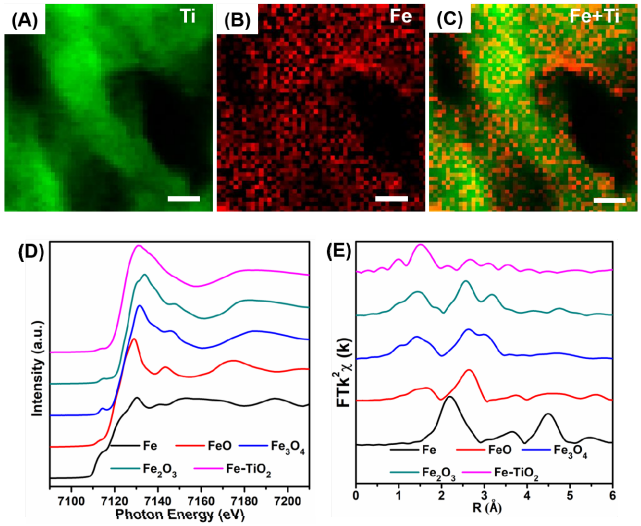

Figure 3. (**A-C**) HAADF-EELS elemental mappings of Fe-TiO_2 (10%) NRs (scale bar: 2 nm); (**D**) Fe K-edge XANES and (**E**) Fourier-transform EXAFS spectra of Fe-TiO_2 (10%) and reference standards.

The dopant distribution within NRs was first studied by STEM high-angle annular dark field (HAADF) images coupled with electron energy loss spectroscopy (EELS) elemental mappings (**Figure 3A-C**, **S9-S11**). It is clearly seen that the dopants, including Fe mono-dopant, bi-M and tri-M, are homogeneously distributed within NRs. To further uncover the atomic arrangement and bonding configuration of M, we performed X-ray absorption near edge structure (XANES) and extended X-ray absorption fine structure (EXAFS) studies. **Figure 3D** displays the Fe K-edge XANES spectra of Fe-TiO_2 NRs as well as reference samples, including Fe, FeO, Fe_3O_4, and Fe_2O_3. The Fe-TiO_2 spectrum is clearly distinct to those of metallic Fe, excluding the existence of the interstitial dopant of Fe in the TiO_2 lattice. Meanwhile, the Fe-TiO_2 shows similar white line characteristics with those of FeO_x, indicating the high valence state of Fe (+3) in the Fe-TiO_2 NRs. Additionally, the observed spectra present different profiles at the range of 7120-7160 eV, implying that the state of Fe in Fe-TiO_2 differs from that in FeO_x. We ascribe these differences to the replacement of Fe in the TiO_2 lattice, which is due to the similarity in the ionic radii of Fe^{3+} (0.064 nm) and Ti^{4+} (0.068 nm).[48] Doping of Fe in the TiO_2 lattice alters the hybridization of Fe with O, inducing a different Fe–O bond environment compared with that in FeO_x. Thus, it is clear that Fe is atomically doped into the TiO_2 without forming any FeO_x segregation.

Moreover, the Fe K-edge EXAFS spectrum of the Fe-TiO_2 along with the spectra of reference samples are presented in **Figure 3E**. We found that Fe-TiO_2 does not have the Fe–Fe bond due to the absence of a peak at 2.21 Å which is an indicator of Fe–Fe bonding observed in metallic Fe foil. Instead, a peak at 1.49 Å, due to the Fe–O bond, is observed in the Fe-TiO_2 spectrum. The peak position is different for FeO (1.57 Å), Fe_3O_4 (1.43 Å), and Fe_2O_3 (1.42 Å). More obviously, the second and third nearest neighboring coordination shells of Fe in the range of 2 – 4 eV of

Fe-TiO_2 are much weaker compared to those in the FeO_x spectra. This reveals again that the existence of Fe metal and Fe oxide secondary phases in the samples can be excluded, and indicates that Fe is distributed in the TiO_2 network as single atoms. The EXAFS studies of other M-TiO_2 (**Figure S12)** also show that single-atom M occupies the Ti site in TiO_2, confirming the universality of atomic doping in the present synthesis.

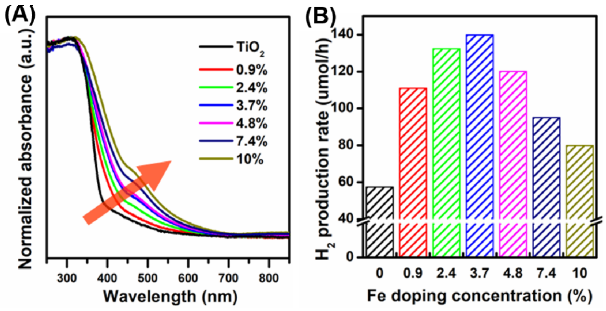

Figure 4. (**A**) UV-vis diffuse reflectance spectra and (**B**) photocatalytic H_2 production of TiO_2 and Fe-TiO_2 NRs with different dopant concentrations.

As illustrated in previous studies on rutile and anatase TiO_2, the t_{2g} state of M dopants can interact with Ti, generating additional occupied state in the bandgap of TiO_2 and tuning the electronic structure of TiO_2.[49] As shown in **Figure 1** and **S13**, our M-TiO_2 NR suspensions in hexanes exhibit distinct colors from TiO_2 (white), suggesting similar electronic structure modification in brookite-phase TiO_2. The absorption edge of brookite-phase TiO_2 NRs is at ~380 nm in the Ultraviolet–visible (UV-Vis) diffuse reflectance spectrum (**Figure 4A**) corresponding to a band gap of ~3.3 eV. For Fe-TiO_2, it can be seen that the Fe dopant shifts the absorption edge of TiO_2 towards longer wavelength. Therefore, the present synthetic strategy offers an effective method to improve the visible-light absorption of pristine TiO_2 NRs.

To illustrate one potential impact of our general synthesis, we selected the photocatalytic H_2 production via methanol reforming as a model reaction and investigated Fe-TiO_2 NRs performance (SI). The pristine TiO_2 brookite-phase NRs, after removing the surfactants using the $NOBF_4$ treatment [50] and photo-depositing 1 wt% Pt co-catalyst, [44, 51] show a hydrogen production rate of ~57 umol/h under 300 W Xenon lamp illumination (**Figure 4B**). Interestingly, all the Fe-TiO_2 NRs with different Fe dopant levels show higher H_2 production rates under the same conditions. The H_2 production rate of the 3.7% Fe-TiO_2 reaches ~140 umol/h corresponding to a ~2.5-time enhancement compared to that of pristine TiO_2 NRs. Such an enhancement is encouraging, given the fact that the pristine TiO_2 brookite-phase NRs have already been demonstrated as one of the most active photocatalysts.[43, 44] Increasing Fe doping level beyond 3.7% results in decreased activity. The enhanced activity of Fe-TiO_2 probably originates from the improved light utilization in the visible range. However, the dopant atoms can also act as charge recombination sites that compromise the charge separation efficiency, which becomes an issue at higher Fe amounts.[40] Thus, an optimal doping concentration for photocatalytic hydrogen production is observed with 3.7% Fe. Meanwhile, it was observed that H_2 production rate only decreased slightly after a 16-hour reaction (**Figure S14**). The Fe-TiO_2 structure and morphology are also well-maintained after catalysis, as indicated by the XRD patterns, TEM images and EELS elemental mappings (**Figure S15** and **S16**), demonstrating the excellent stability of the Fe-TiO_2 NR photocatalyst.

This communication highlights a generalized synthetic strategy for doped M-TiO_2 NRs with consistent brookite phase, quadrangular 1-D morphology, and controllable dopant compositions and concentrations. Photocatalytic H_2 production based on the resultant Fe-TiO_2 NRs demonstrates the Fe-doping can lead to a substantial catalytic activity enhancement probably due to a dopant-induced optical absorption improvement. The unique capability of our synthetic approach in preparing more improved photocatalysts will be further investigated in our follow-up study of M-TiO_2 NRs with diverse M compositions/concentrations. In addition, the present M-TiO_2 NRs may allow additional opportunities in heterogeneous catalysis, serving as a new type of either catalytic materials with single-atom M sites or catalyst supports with tunable electronic structure, lattice oxygen activity and surface acidity/basicity.

ASSOCIATED CONTENT

Supporting Information
Materials and Method, Scheme S1, **Table S1**, **Figures S1-16** are presented in the supporting information. This material is available free of charge via the Internet at http://pubs.acs.org.

AUTHOR INFORMATION

Corresponding Author
E-mail for D. S.: dsu@bnl.gov
E-mail for S. Z.: sz3t@virginia.edu

ORCID
Dong Su: 0000-0002-1921-6683
Sen Zhang: 0000-0002-1716-3741

Author Contributions
Z. Zhang, Q. Wu and G. Johnson contributed equally to this work.

ACKNOWLEDGMENTS. This work was supported by U. S. National Science Foundation (CBET-1805022). Partial work on electron microscopy carried out the Center for Functional Nanomaterials, which is a U.S. DOE Office of Science Facility, at Brookhaven National Laboratory under Contract No. DE-SC0012704. We appreciate the experimental support from Sirine Fakra at the Advanced Light Source. The Advanced Light Source is supported by the Director, Office of Science, Office of Basic Energy Sciences, of the U.S. Department of Energy under Contract No. DE-AC02-05CH1123. C.B.M and J.D.L acknowledge the partial support provided by the Vagelos Institute of Energy Science and Technology at the University of Pennsylvania.

REFERENCES

1. Gilroy, K. D.; Ruditskiy, A.; Peng, H.-C.; Qin, D.; Xia, Y., Bimetallic Nanocrystals: Syntheses, Properties, and Applications. *Chem. Mater.* **2016,** *116*, 10414.
2. Wu, Y.; Wang, D.; Li, Y., Nanocrystals from Solutions: Catalysts. *Chem. Soc. Rev.* **2014,** *43*, 2112.
3. Zhou, Z.-Y.; Tian, N.; Li, J.-T.; Broadwell, I.; Sun, S.-G., Nanomaterials of High Surface Energy with Exceptional Properties in Catalysis and Energy Storage. *Chem. Soc. Rev.* **2011,** *40*, 4167.
4. Cargnello, M.; Gordon, T. R.; Murray, C. B., Solution-Phase Synthesis of Titanium Dioxide Nanoparticles and Nanocrystals. *Chem. Mater.* **2014,** *114*, 9319.
5. Wang, L.; Holewinski, A.; Wang, C., Prospects of Platinum-Based Nanostructures for the Electrocatalytic Reduction of Oxygen. *ACS Cata.* **2018,** *8*, 9388.
6. Xia, Y.; Yang, H.; Campbell, C. T., Nanoparticles for Catalysis. *Acc. Chem. Res.* **2013,** *46*, 1671.
7. Xu, L.; Liang, H.-W.; Yang, Y.; Yu, S.-H., Stability and Reactivity: Positive and Negative Aspects for Nanoparticle Processing. *Chem. Rev.* **2018,** *118*, 3209.
8. Hahn, R.; Schmidt-Stein, F.; Salonen, J.; Thiemann, S.; Song, Y.; Kunze, J.; Lehto, V.-P.; Schmuki, P., Semimetallic TiO_2 Nanotubes. *Angew. Chem. Int. Ed.* **2009,** *48*, 7236.
9. Roy, P.; Berger, S.; Schmuki, P., TiO_2 Nanotubes: Synthesis and Applications. *Angew. Chem. Int. Ed.* **2011,** *50*, 2904.

10. Bai, J.; Zhou, B., Titanium Dioxide Nanomaterials for Sensor Applications. *Chem. Rev.* **2014,** *114*, 10131.
11. Cargnello, M.; Gordon, T. R.; Murray, C. B., Solution-Phase Synthesis of Titanium Dioxide Nanoparticles and Nanocrystals. *Chem. Rev.* **2014,** *114*, 9319.
12. Yang, H. G.; Sun, C. H.; Qiao, S. Z.; Zou, J.; Liu, G.; Smith, S. C.; Cheng, H. M.; Lu, G. Q., Anatase TiO_2 Single Crystals with a Large Percentage of Reactive Facets. *Nature* **2008,** *453*, 638.
13. Gordon, T. R.; Cargnello, M.; Paik, T.; Mangolini, F.; Weber, R. T.; Fornasiero, P.; Murray, C. B., Nonaqueous Synthesis of TiO2 Nanocrystals Using TiF_4 to Engineer Morphology, Oxygen Vacancy Concentration, and Photocatalytic Activity. *J. Am. Chem. Soc.* **2012,** *134*, 6751.
14. Buonsanti, R.; Grillo, V.; Carlino, E.; Giannini, C.; Kipp, T.; Cingolani, R.; Cozzoli, P. D., Nonhydrolytic Synthesis of High-Quality Anisotropically Shaped Brookite TiO_2 Nanocrystals. *J. Am. Chem. Soc.* **2008,** *130*, 11223.
15. Qin, D.-D.; Bi, Y.-P.; Feng, X.-J.; Wang, W.; Barber, G. D.; Wang, T.; Song, Y.-M.; Lu, X.-Q.; Mallouk, T. E., Hydrothermal Growth and Photoelectrochemistry of Highly Oriented, Crystalline Anatase TiO2 Nanorods on Transparent Conducting Electrodes. *Chem. Mater.* **2015,** *27*, 4180.
16. Bai, Y.; Mora-Seró, I.; De Angelis, F.; Bisquert, J.; Wang, P., Titanium Dioxide Nanomaterials for Photovoltaic Applications. *Chem. Mater.* **2014,** *114*, 10095.
17. Gao, X.; Li, G.; Xu, Y.; Hong, Z.; Liang, C.; Lin, Z., TiO_2 Microboxes with Controlled Internal Porosity for High-Performance Lithium Storage. *Angew. Chem. Int. Ed.* **2015,** *54*, 14331.
18. Yu, X.-Y.; Wu, H. B.; Yu, L.; Ma, F.-X.; Lou, X. W., Rutile TiO_2 Submicroboxes with Superior Lithium Storage Properties. *Angew. Chem. Int. Ed.* **2015,** *54*, 4001.
19. Singh, D. P.; George, A.; Kumar, R. V.; ten Elshof, J. E.; Wagemaker, M., Nanostructured TiO_2 Anatase Micropatterned Three-Dimensional Electrodes for High-Performance Li-Ion Batteries. *J. Phys. Chem. C* **2013,** *117*, 19809.
20. Pepin, P. A.; Diroll, B. T.; Choi, H. J.; Murray, C. B.; Vohs, J. M., Thermal and Photochemical Reactions of Methanol, Acetaldehyde, and Acetic Acid on Brookite TiO_2 Nanorods. *J. Phys. Chem. C* **2017,** *121*, 11488.
21. Enache, D. I.; Edwards, J. K.; Landon, P.; Solsona-Espriu, B.; Carley, A. F.; Herzing, A. A.; Watanabe, M.; Kiely, C. J.; Knight, D. W.; Hutchings, G. J., Solvent-free Oxidation of Primary Alcohols to Aldehydes Using Au-Pd/TiO_2 Catalysts. *Science* **2006,** *311*, 362.
22. Linsebigler, A. L.; Lu, G.; Yates, J. T., Photocatalysis on TiO_2 Surfaces: Principles, Mechanisms, and Selected Results. *Chem. Mater.* **1995,** *95*, 735.
23. Wang, C. J.; Thompson, R. L.; Ohodnicki, P.; Baltrus, J.; Matranga, C., Size-dependent photocatalytic reduction of CO_2 with PbS quantum dot sensitized TiO2 heterostructured photocatalysts. *J. Mater. Chem.* **2011,** *21*, 13452.
24. Dhakshinamoorthy, A.; Navalon, S.; Corma, A.; Garcia, H., Photocatalytic CO_2 Reduction by TiO_2 and Related Titanium Containing Solids. *Energy Environ. Sci.* **2012,** *5*, 9217.
25. Hu, J.-L.; Qian, H.-S.; Li, J.-J.; Hu, Y.; Li, Z.-Q.; Yu, S.-H., Synthesis of Mesoporous SiO_2@TiO_2 Core/Shell Nanospheres with Enhanced Photocatalytic Properties. *Part. Part. Syst. Charact.* **2013,** *30*, 306.
26. Ting, K. W.; Toyao, T.; Siddiki, S. M. A. H.; Shimizu, K.-i., Low-Temperature Hydrogenation of CO2 to Methanol over Heterogeneous TiO2-Supported Re Catalysts. *ACS Catalysis* **2019,** *9*, 3685.
27. Widmann, D.; Behm, R. J., Active Oxygen on a Au/TiO2 Catalyst: Formation, Stability, and CO Oxidation Activity. *Angew. Chem. Int. Ed.* **2011,** *50*, 10241.
28. Arrii, S.; Morfin, F.; Renouprez, A. J.; Rousset, J. L., Oxidation of CO on Gold Supported Catalysts Prepared by Laser Vaporization: Direct Evidence of Support Contribution. *J. Am. Chem. Soc.* **2004,** *126*, 1199.
29. Fujishima, A.; Honda, K., Electrochemical Photolysis of Water at a Semiconductor Electrode. *Nature* **1972,** *238*, 37.
30. Li, Y. F.; Selloni, A., Pathway of Photocatalytic Oxygen Evolution on Aqueous TiO_2 Anatase and Insights into the Different Activities of Anatase and Rutile. *ACS Catal.* **2016,** *6*, 4769.
31. Lee, C.-Y.; Park, H. S.; Fontecilla-Camps, J. C.; Reisner, E., Photoelectrochemical H_2 Evolution with a Hydrogenase Immobilized on a TiO_2-Protected Silicon Electrode. *Angew. Chem. Int. Ed.* **2016,** *55*, 5971.
32. Ni, M.; Leung, M. K. H.; Leung, D. Y. C.; Sumathy, K., A review and recent developments in photocatalytic water-splitting using TiO_2 for hydrogen production. *Renewable Sustainable Energy Rev.* **2007,** *11*, 401.
33. Choi, W.; Termin, A.; Hoffmann, M. R., The Role of Metal Ion Dopants in Quantum-Sized TiO_2: Correlation between Photoreactivity and Charge Carrier Recombination Dynamics. *J. Phys. Chem.* **1994,** *98*, 13669.
34. Cao, Y.; He, T.; Chen, Y.; Cao, Y., Fabrication of Rutile TiO_2−Sn/Anatase TiO_2−N Heterostructure and Its Application in Visible-Light Photocatalysis. *J. Phys. Chem. C* **2010,** *114*, 3627.
35. Dong, F.; Guo, S.; Wang, H.; Li, X.; Wu, Z., Enhancement of the Visible Light Photocatalytic Activity of C-Doped TiO_2 Nanomaterials Prepared by a Green Synthetic Approach. *J. Phys. Chem. C* **2011,** *115*, 13285.
36. Burda, C.; Lou, Y.; Chen, X.; Samia, A. C. S.; Stout, J.; Gole, J. L., Enhanced Nitrogen Doping in TiO_2 Nanoparticles. *Nano Letters* **2003,** *3*, 1049.
37. Yu, J. C.; Yu; Ho; Jiang; Zhang, Effects of F- Doping on the Photocatalytic Activity and Microstructures of Nanocrystalline TiO_2 Powders. *Chem. Mater.* **2002,** *14*, 3808.
38. In, S.-I.; Vaughn Ii, D. D.; Schaak, R. E., Hybrid CuO-$TiO_{2-x}N_x$ Hollow Nanocubes for Photocatalytic Conversion of CO_2 into Methane under Solar Irradiation. *Angew. Chem. Int. Ed.* **2012,** *51*, 3915.
39. Xu, L.; Steinmiller, E. M. P.; Skrabalak, S. E., Achieving Synergy with a Potential Photocatalytic Z-Scheme: Synthesis and Evaluation of Nitrogen-Doped TiO_2/SnO_2 Composites. *J. Phys. Chem. C* **2012,** *116*, 871.
40. Schneider, J.; Matsuoka, M.; Takeuchi, M.; Zhang, J.; Horiuchi, Y.; Anpo, M.; Bahnemann, D. W., Understanding TiO_2 Photocatalysis: Mechanisms and Materials. *Chem. Rev.* **2014,** *114*, 9919.
41. Liu, B.; Chen, H. M.; Liu, C.; Andrews, S. C.; Hahn, C.; Yang, P., Large-Scale Synthesis of Transition-Metal-Doped TiO2 Nanowires with Controllable Overpotential. *J. Am. Chem. Soc.* **2013,** *135*, 9995.
42. Du, Q.; Wu, J.; Yang, H., Pt@Nb-TiO_2 Catalyst Membranes Fabricated by Electrospinning and Atomic Layer Deposition. *ACS Cata.* **2014,** *4*, 144.
43. Cargnello, M.; Montini, T.; Smolin, S. Y.; Priebe, J. B.; Delgado Jaén, J. J.; Doan-Nguyen, V. V. T.; McKay, I. S.; Schwalbe, J. A.; Pohl, M.-M.; Gordon, T. R.; Lu, Y.; Baxter, J. B.; Brückner, A.; Fornasiero, P.; Murray, C. B., Engineering Titania Nanostructure to Tune and Improve its Photocatalytic Activity. *Proc. Natl. Acad. Sci. U.S.A.* **2016,** *113*, 3966.
44. Pepin, P. A.; Lee, J. D.; Murray, C. B.; Vohs, J. M., Thermal and Photocatalytic Reactions of Methanol and Acetaldehyde on Pt-Modified Brookite TiO_2 Nanorods. *ACS Catal.* **2018,** *8*, 11834.
45. Park, J.; An, K.; Hwang, Y.; Park, J.-G.; Noh, H.-J.; Kim, J.-Y.; Park, J.-H.; Hwang, N.-M.; Hyeon, T., Ultra-Large-Scale Syntheses of Monodisperse Nanocrystals. *Nat. Mater.* **2004,** *3*, 891.
46. Dong, A.; Chen, J.; Vora, P. M.; Kikkawa, J. M.; Murray, C. B., Binary nanocrystal superlattice membranes self-assembled at the liquid–air interface. *Nature* **2010,** *466*, 474.
47. Gong, X.-Q.; Selloni, A., First-Principles Study of the Structures and Energetics of Stoichiometric Brookite TiO_2 Surfaces. *Phys. Rev. B* **2007,** *76*, 235307.
48. Açıkgöz, M.; Gnutek, P.; Rudowicz, C., Modeling Zero-Eield Splitting Parameters for Dopant Mn^{2+} and Fe^{3+} Ions in Anatase TiO_2 Crystal using Superposition Model Analysis. *Chem. Phys. Lett.* **2012,** *524*, 49.
49. Park, M. S.; Kwon, S. K.; Min, B. I., Electronic Structures of Doped Anatase TiO_2: $Ti_{1-x}M_xO_2$ (M = Co, Mn, Fe, Ni). *Phys. Rev. B* **2002,** *65*, 161201.
50. Dong, A.; Ye, X.; Chen, J.; Kang, Y.; Gordon, T.; Kikkawa, J. M.; Murray, C. B., A Generalized Ligand-Exchange Strategy

Enabling Sequential Surface Functionalization of Colloidal Nanocrystals. *J. Am. Chem. Soc.* **2011,** *133*, 998.

51. Wu, Q.; Xiong, S.; Shen, P.; Zhao, S.; Li, Y.; Su, D.; Orlov, A., Exceptional activity of sub-nm Pt clusters on CdS for photocatalytic hydrogen production: a combined experimental and first-principles study. *Catal. Sci. Technol.* **2015,** *5*, 2059.

TOC

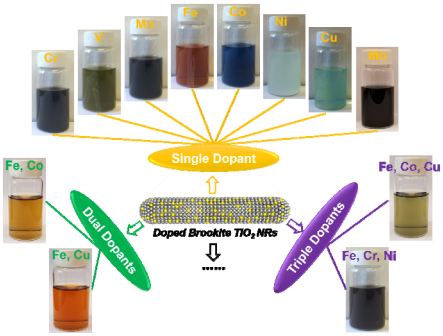
Cr
V
Mn
Fe
Co
Ni
Cu
Mo
Single Dopant
Fe, Co
Dual Dopants
Fe, Cu
Doped Brookite TiO2 NRs
Triple Dopants
Fe, Co, Cu
Fe, Cr, Ni
.....

Supporting Information

Generalized Synthetic Strategy for Transition Metal Doped Brookite-Phase TiO_2 Nanorods

Zhiyong Zhang[1,#], Qiyuan Wu[2,#], Grayson Johnson[1,#], Yifan Ye[3], Xing Li[4], Na Li[4], Meiyang Cui[1], Jennifer D. Lee[5], Chang Liu[1], Shen Zhao[4], Shuang Li[4], Alexander Orlov[2], Christopher B. Murray[5], Xu Zhang[6], T. Brent Gunnoe[1], Dong Su[4,*], Sen Zhang[1,*]

[1]Department of Chemistry, University of Virginia, Charlottesville, Virginia 22904, USA;
[2]Department of Materials Science and Chemical Engineering, State University of New York, Stony Brook, New York 11794, USA;
[3]Advanced Light Source, Lawrence Berkeley National Laboratory, Berkeley, California 94720, USA;
[4]Center for Functional Nanomaterials, Brookhaven National Laboratory, Upton, New York 11973, USA;
[5]Department of Chemistry, University of Pennsylvania, Philadelphia, Pennsylvania 19104, USA;
[6]Department of Physics and Astronomy, California State University Northridge, Northridge, California 91330, USA.

*To whom correspondence should be addressed.

E-mail for D. S.: dsu@bnl.gov

E-mail for S. Z.: sz3t@virginia.edu

This file includes:

Materials and Methods

Materials

Oleylamine (OAm, 70%) and oleic acid (OAc, 90%) were purchased from Sigma-Aldrich. Octadecene (ODE, 90%), cobalt(II) acetylacetonate ($Co(acac)_2$, 99%), nickel(II) acetylacetonate ($Ni(acac)_2$, 96%), copper(II) acetylacetonate ($Cu(acac)_2$, 98%) and titanium chloride ($TiCl_4$, 99.9%) were obtained from Acros Organics. Iron(III) chloride anhydrous ($FeCl_3$, 98%), vanadium(III) chloride (VCl_3, 99%), chromium(III) chloride, anhydrous ($CrCl_3$, 98%) were purchased from Alfa Aesar. Manganese(II) chloride anhydrous ($MnCl_2$, 97%), molybdenum(V) chloride anhydrous ($MoCl_5$, 99.6%) were obtained from Stream Chemical. Diethylene glycol (DEG, Reagent Grade) was purchased from Fisher Scientific.

Synthesis of TiO_2 NRs

Brookite-phase TiO_2 NRs were synthesized via a colloidal approach, based on a modification of previous publications.[1-2] To obtain TiO_2 NRs, 10 ml of ODE, 10 ml of OAm and 0.48 ml OAc were first heated under vacuum at 90 °C for one hour to remove dissolved moisture and oxygen. After that, the mixture was cooled down to 60 °C under nitrogen and 1.5 ml of Ti-precursor solution containing 0.2 M $TiCl_4$ and 1.0 M OAc in ODE was injected into the solution (ODE and OAc should be pre-dried to avoid undesirable $TiCl_4$ hydrolysis). The system was then quickly heated up to 290 °C and held at that temperature for 10 min. Next, 8 mL of additional Ti precursor solution was added dropwise into the reactor at a rate of 0.3 mL min^{-1}. Note that this solution, when heated, is corrosive due to the generation of HCl, and any unwanted metal sources like metal temperature probes should be avoided. After being cooled down to room temperature, the TiO_2 NRs were collected and washed by the addition of isopropanol and subsequent centrifugation at 8000 rpm for 8 min. The product was further purified twice by the addition of hexane and isopropanol.

Preparation of M-oleate precursor solution

The M-oleate solution was prepared by dissolving the as-received metal precursor (MCl_x or $M(acac)_x$) into a mixture of OAc and ODE. For example, to prepare a Fe-oleate solution, 3.24 g of $FeCl_3$ was dissolved into a mixture of 31.59 ml of pre-dried OAc and 68.41 ml of pre-dried ODE at 100°C in a N_2-filled glovebox to yield 0.2 M Fe oleate in OAc/ODE solution. By using 5.14 g of $Co(acac)_2$, 5.13 g of $Ni(acac)_2$, 5.23 g of $Cu(acac)_2$, 3.15 g of VCl_3, 3.17 g of $CrCl_3$, 2.52 g of $MnCl_2$, 5.46 g of $MoCl_5$ instead of $FeCl_3$, other M-oleate solutions with 0.2 M M-oleate were made. As chemical composition and concentration of these M-oleate solutions are similar to the Ti-precursor solution, they can be well-mixed with the Ti-precursor solution at any desired level, enabling the facile synthesis of M-TiO_2 NRs, as described in the following session.

Synthesis of M-TiO_2 NRs

M-TiO_2 NRs were synthesized via approaches similar to that for pristine TiO_2 NRs, except $TiCl_4$ – M-oleate mixed solution was used. For example, to prepare Fe-TiO_2 NRs, the Fe-oleate precursor solution was mixed with the Ti-precursor solution with a desired Ti/Fe ratio. 1.5 ml of this mixed solution was injected into the degassed solution containing 10 ml of ODE, 10 ml of OAm, and 0.48 ml of OAc at 60°C, and was quickly heated up to 290°C. After being held at that temperature for 10 min, another 8 ml of the $TiCl_4$ – Fe-oleate mixed solution was dropwisely introduced into the system at 0.3 ml min^{-1}. The as-prepared Fe-TiO_2 was collected and purified via the same way for pristine TiO_2 NRs. In this synthesis, the Fe doping level in TiO_2 NRs was tuned by altering Ti/Fe ratio in the mixed precursor solution. For example, by tuning Ti/Fe precursor ratio from 8/1 to 8/0.75, 8/0.5, 8/0.38, 8/0.25, and 8/0.1, a Fe doping level of 10%, 7.4%, 4.8%,

3.7%, 2.4%, and 0.9% were achieved in TiO_2 NRs. Simply replacing Fe-oleate with other M-oleate solution (M = V, Cr, Mn, Co, Ni, Cu, Mo) in this procedure will yield other M-TiO_2 NRs with varied M content. Mixing two and three types of M-oleate precursor solutions with $TiCl_4$ precursor led to binary and ternary M-TiO_2 NRs.

Vertical alignment of M-TiO_2 NRs

A typical procedure to fabricate the vertically aligned M-TiO_2 NRs assembly is described in **Scheme S1**. Generally, 60 mg of the as-synthesized M-TiO_2 NRs were dispersed in 10 μl of hexanes, which was transferred on the surface of DEG in a Teflon well. The well was then covered with a glass slide to allow the hexanes to evaporate slowly for 2 hours. After all the hexanes being evaporated, a monolayer vertically aligned M-TiO_2 NR assembly was achieved on the surface of DEG, which can be transferred on any substrate (including TEM grid) by placing it under the NR assembly followed by slowly lifting the substrate. The remaining DEG on the substrate was dried in vacuum oven for overnight.

Surfactant removal from M-TiO_2 NRs

The as-synthesized M-TiO_2 NRs were stabilized with long carbon-chain surface ligands (OAm) to keep the NRs well-dispersed in the storage solution (hexanes). However, the presence of these bulky capping agents creates an inhibiting layer that block the surface active sites and mass transfer during catalysis. To remove this layer, a NOBF ligand exchange was performed according to a previous publication.[3] Typically, 10 ml of the NR dispersion in hexanes (~10 mg ml^{-1}) was mixed with 10 ml of DMF/$NOBF_4$ solution (0.085 M) at room temperature and was vigorously shaken to generate a good mixing between two phases. The NRs were then collected by centrifugation at 8000 rpm for 8 min and was further purified twice by the addition of DMF and hexanes. After the ligand exchange, the as-obtained M-TiO_2 NRs were dried under vacuum for overnight to remove the trace amount of DMF residuals.

Characterization

The structure, morphology, and composition of the as-synthesized TiO_2 and M-TiO_2 NRs were analyzed by X-ray diffraction (XRD), transmission electron microscopy (TEM), high resolution transmission electron microscopy (HR-TEM), scanning transmission electron microscopy (STEM), and X-ray absorption spectroscopy. XRD patterns were collected under a Rigaku Smartlab diffractometer with Cu Kα radiation (λ=1.5418Å). TEM images were obtained on a JEOL 1400 (120 kV). HR-TEM and STEM imaging was performed on analyses were carried out using a Hitachi HD2700C (200kV) with a probe aberration-corrector coupled with EELS and EDS detectors, in the Center for Functional Nanomaterials at Brookhaven National Lab. The EELS mapping and spectrum were collected using a high resolution Gatan-Enfina ER with a probe size of 1.3Å. A power law function was used for EELS background subtraction. Ultraviolet–visible (UV-Vis) diffuse reflectance spectra were collected on Thermo Scientific Evolution 300. The UV-Vis data were further transformed to Tauc plots and the linear regions were extrapolated to analyze the band gaps of TiO_2 and M-TiO_2 NRs

The X-ray absorption spectra, including the near-edge X-ray absorption near-edge structure (XANES) spectra and extended X-ray absorption fine structure (EXAFS) spectra, at the Fe K-edge were recorded at the hard X-ray XAS station (BL 10.3.2) of the Advanced Light Source, Lawrence Berkeley National Laboratory (ALS, LBL). The storage ring was operated at top-off mode (1.9 GeV, 296 buckets, 500 mA). The data collection was carried out in fluorescence mode for the Fe-TiO_2 samples in ambient conditions and transition mode for the reference samples. The beam size was limited by the horizontal and vertical slits with the area of 15 × 3 μm^2 during the measurements. The raw XAS data were processed using Athena

Demeter version 0.9.24. The work-up of raw XAFS data to k-space and Fourier transformed R-space was processed using a consistent methodology of background subtraction, conversion to k-space, and conversion to FT R-space. All sample data was refined using k2-weighting, a k-range of 3 -12 $Å^{-1}$ and R-range of 0-6 Å.

Photocatalysis

Photocatalytic hydrogen production was carried out in a customized reactor equipped with a quartz window. The reactor was connected to a closed gas circulation and evacuation system. For each experiment, 50 mg sample was dispersed in 180 ml aqueous methanol (20 vol%) solution. The system was then purged with ultra-high-purity (UHP) grade Argon gas under stirring for 30 minutes in dark, followed by a degassing procedure. Afterward, 0.8 bar UHP Argon gas was introduced to the system as carrier gas. The suspension was then illuminated by a 300W Xe lamp (Newport, Model 66984) which was equipped with a high pass cutoff filter to eliminate light with $\lambda < 320$ nm and a 10 cm water filter (> 800 nm) to eliminate IR irradiation. During the catalysis, 1 wt% of Pt co-catalyst was loaded by *in-situ* photo-deposition using the proper amount of H_2PtCl_6.[4-5] The gas products were quantified by using an online gas chromatography (Agilent, 7890A) which was equipped with a thermal conductivity detector (TCD) and a 5 Å molecular sieve column.

Computational Details

DFT Calculations were performed with the Vienna ab initio simulation package (VASP)[6] with the projector augmented-wave (PAW) pseudopotentials[7] and the revised Perdew-Burke-Ernzerhof (RPBE) exchange correlation functional.[8] An energy cutoff of 400 eV was used for the plane wave basis set. The DFT-D3 of Grimme for dispersion correction was applied.[9] All calculations were spin polarized. The force convergence criterion was 0.02 eV $Å^{-1}$ and the energy convergence criterion was 10^{-5} eV for geometry optimizations.

The (210) surface of a brookite-phase TiO_2 was modeled by a (2×1) unit slab with 35 Å of vacuum normal to the surface. The atoms in the top three layers and adsorbate were fully relaxed while the rest of the atoms were fixed in their equilibrium positions. The supercell was sampled with a 3 x 1 x 1 Monkhorst Pack k-point mesh.[10] The (001) surface was built with a (2×2) unit slab and a 3 x 5 x 1 Monkhorst Pack k-point mesh was sampled. The binding energy between each adsorbate (oleylamine, oleic acid, oleate, and Cl) and the TiO_2 surface was calculated by

$$E_{Ads} = E(Adsorbate + Slab) - E(Slab) - E(Adsorbate) \qquad (0.1)$$

Here E(Adsorbate+Slab) is the total energy of the TiO_2 slab with adsorbate. E[slab] is the total energy of the TiO_2 slab. E[Adsorbate] is the total energy of fully relaxed adsorbate molecules (oleylamine or oleic acid) or Cl atom. The brookite TiO_2(001) surface has a local minimum structure accessible from geometry relaxations of the as built system. However, the (001) surface undergoes 1x1 reconstruction which become more energetically stable. This surface reconstruction has been reported by Gong *et al*.[11] In our calculations, the (001) surface was manually rebuilt and structurally minimized to generate the reconstruction (Figure S8), and all adsorption energies on the (001) surface were reported with reference to the reconstructed surface.

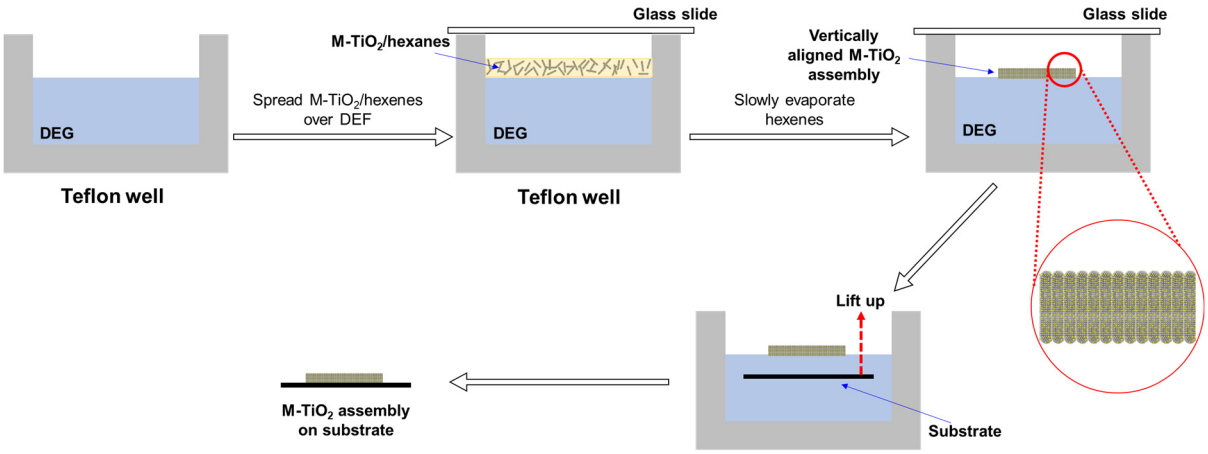

Scheme S1. Fabrication and transferring of vertically aligned M-TiO_2 assembly.

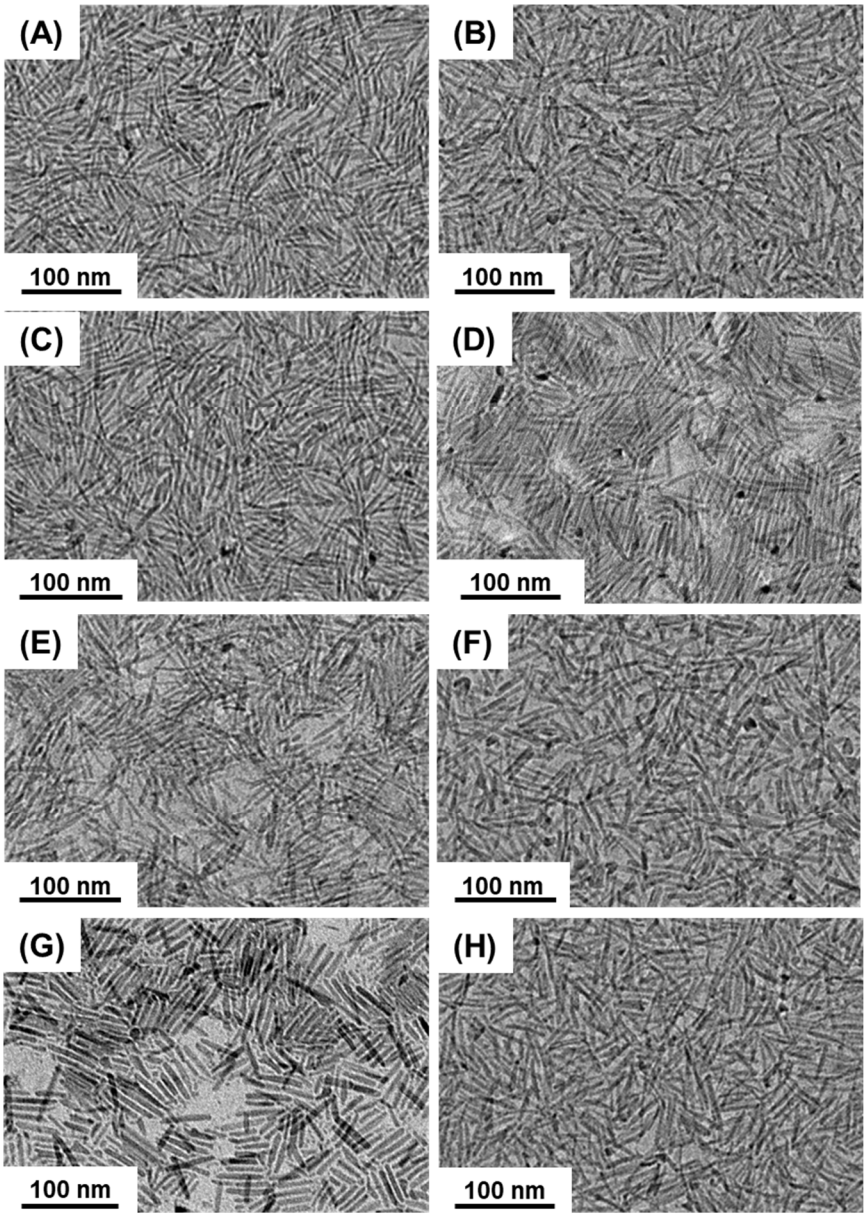

Figure S1. (**A-H**) TEM images of (**A**) pristine TiO_2, (**B**) V-TiO_2, (**C**) Mn-TiO_2, (**D**) Co-TiO_2, (**E**) Ni-TiO_2, (**F**) Cu-TiO_2, (**G**) Mo-TiO_2 (all around 10% M dopant concentration), (**H**) 3.7% Fe-TiO_2 NRs.

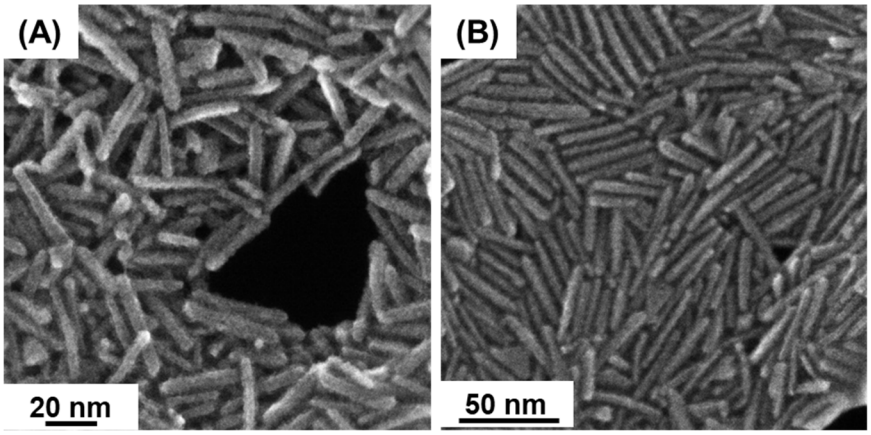

Figure S2. STEM images of (**A**) Fe-TiO_2 (10% Fe) and (**B**) TiO_2 NRs.

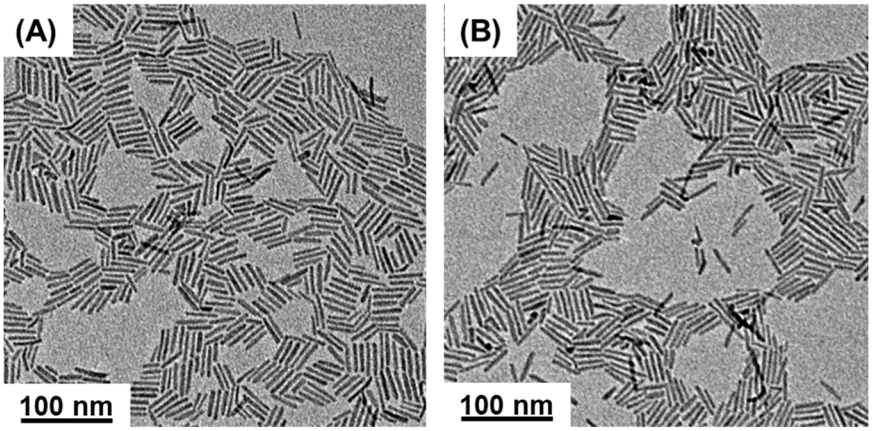

Figure S3. TEM images of bi-M-TiO_2 NRs: (**A**) FeCo-TiO_2, (**B**) FeCu-TiO_2.

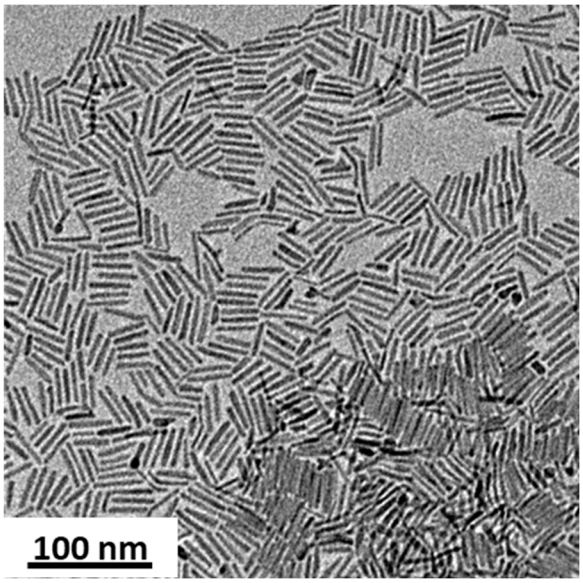

Figure S4. TEM images of FeCoCu-TiO_2 NRs.

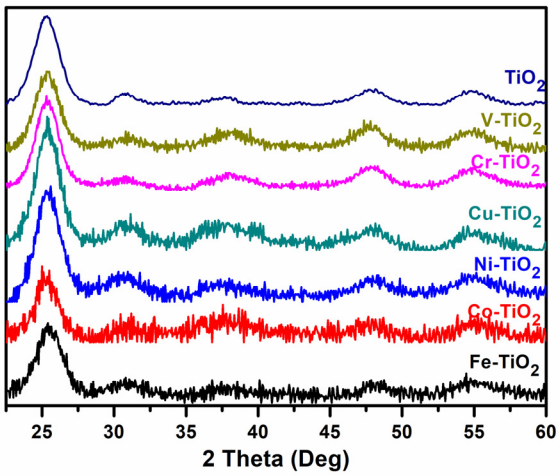

Figure S5. X-ray diffraction patterns of TiO_2 and M-TiO_2 NRs (10% M).

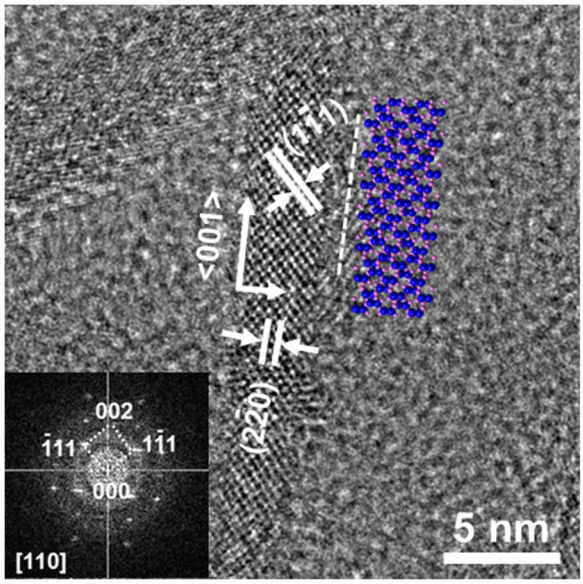

Figure S6. HRTEM image of pristine TiO_2 NRs. Inset illustrates the corresponding atomic model with purple and pink atoms being Ti and O. Inset also shows fast Fourier transform of HRTEM image.

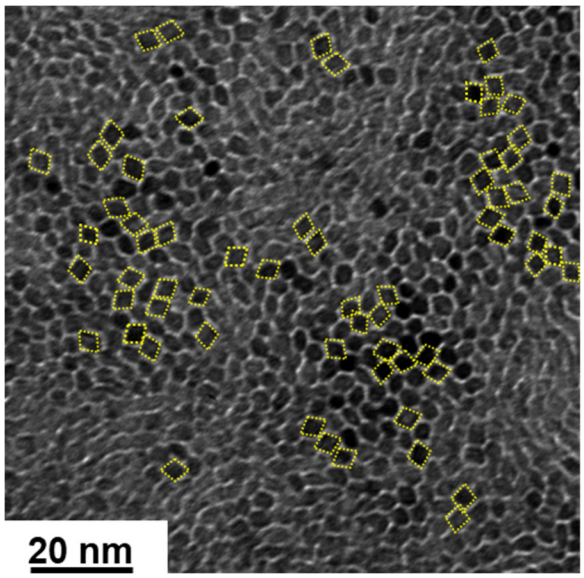

Figure S7. TEM image of vertically aligned pristine TiO_2 NRs assembly.

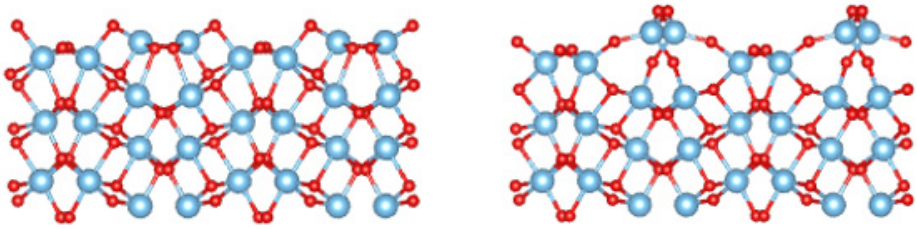

Figure S8. DFT models of the (001) brookite TiO_2 surface before (left) and after (right) the 1x1 reconstruction of the surface. The reconstruction is more stable by 38 meV/Å^2 The light blue atoms are Ti while the red atoms are O.

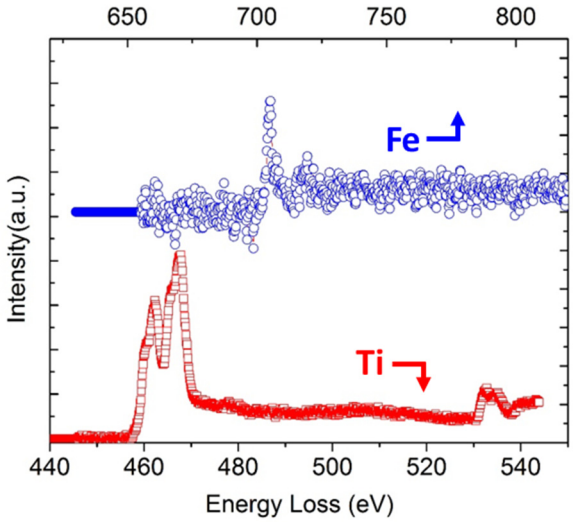

Figure S9. EELS spectra of Fe L-edges and Ti L-edges of Fe-TiO_2 NRs.

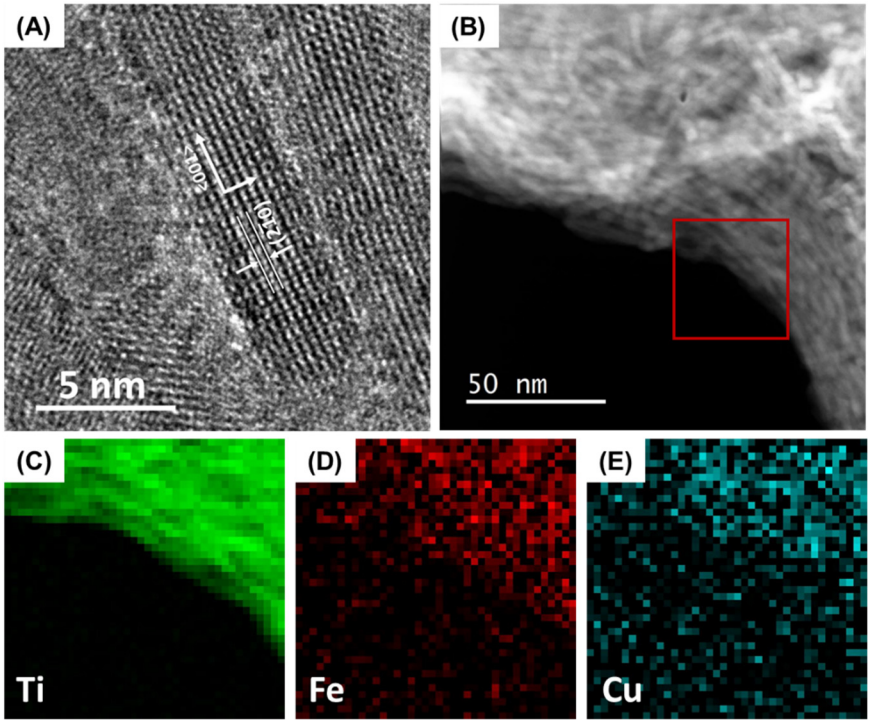

Figure S10. (A) HRTEM and (B) STEM-HAADF images and (C-E) HAADF-EELS 2D mapping of the as-synthesized Fe, Cu-TiO_2 NRs.

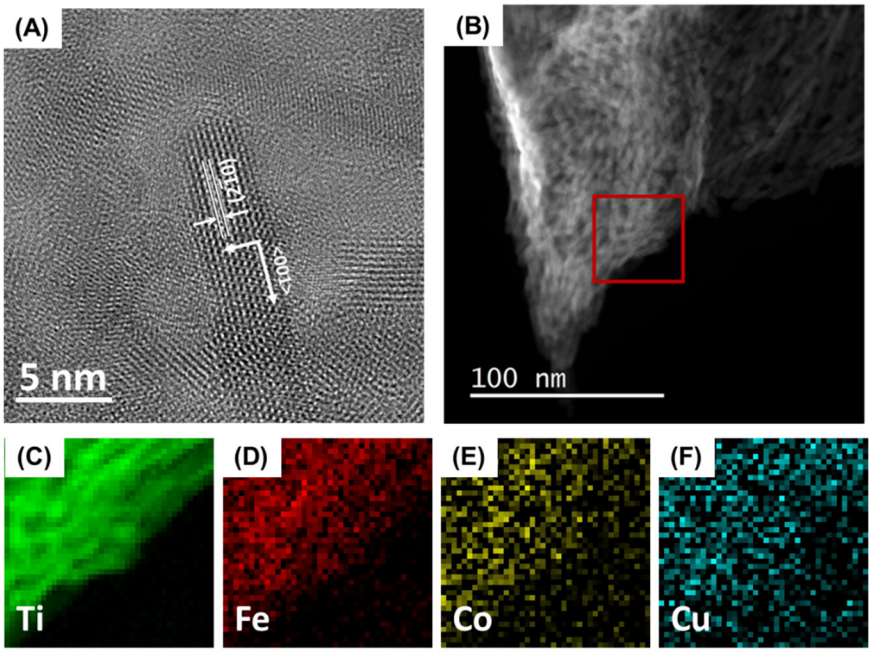

Figure S11. (A) HRTEM and (B) STEM-HAADF images and (C-F) HAADF-EELS mapping of the as-synthesized Fe, Co, Cu-TiO_2 NRs.

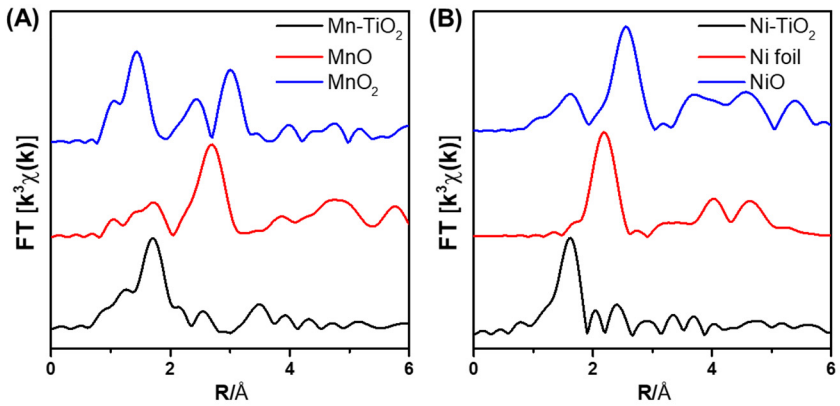

Figure S12. Fourier-transform EXAFS spectra of (A) Mn-TiO_2 and (B) Ni-TiO_2, with 10% M doping level, compared with corresponding standards.

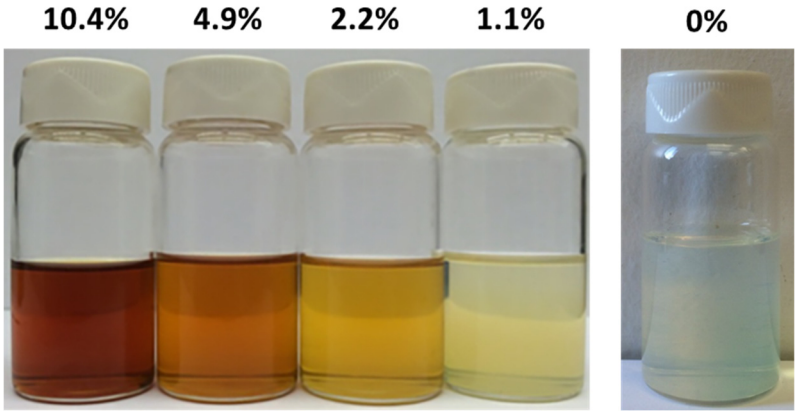

Figure S13. Typical optical images of Fe-TiO_2 with different doping ratios compared with pristine TiO_2 NRs.

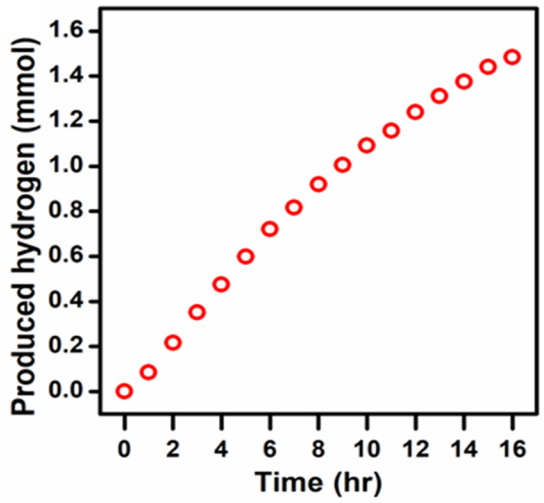

Figure S14. Photocatalytic H_2 production of Fe-TiO_2 NRs with 3.7 wt% Fe doping.

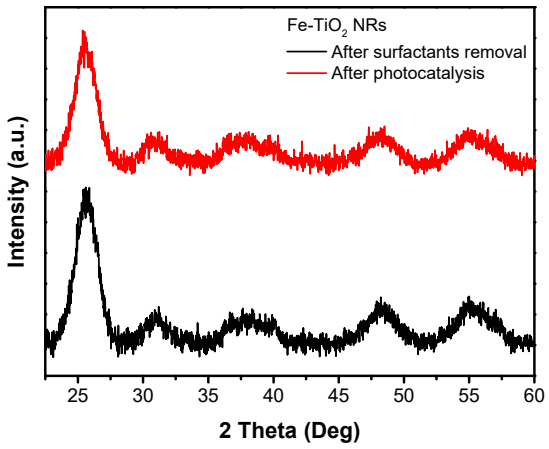

Figure S15. X-ray diffraction patterns of Fe-TiO_2 (10% Fe) after surfactants removal and a 16-hour photocatalysis testing.

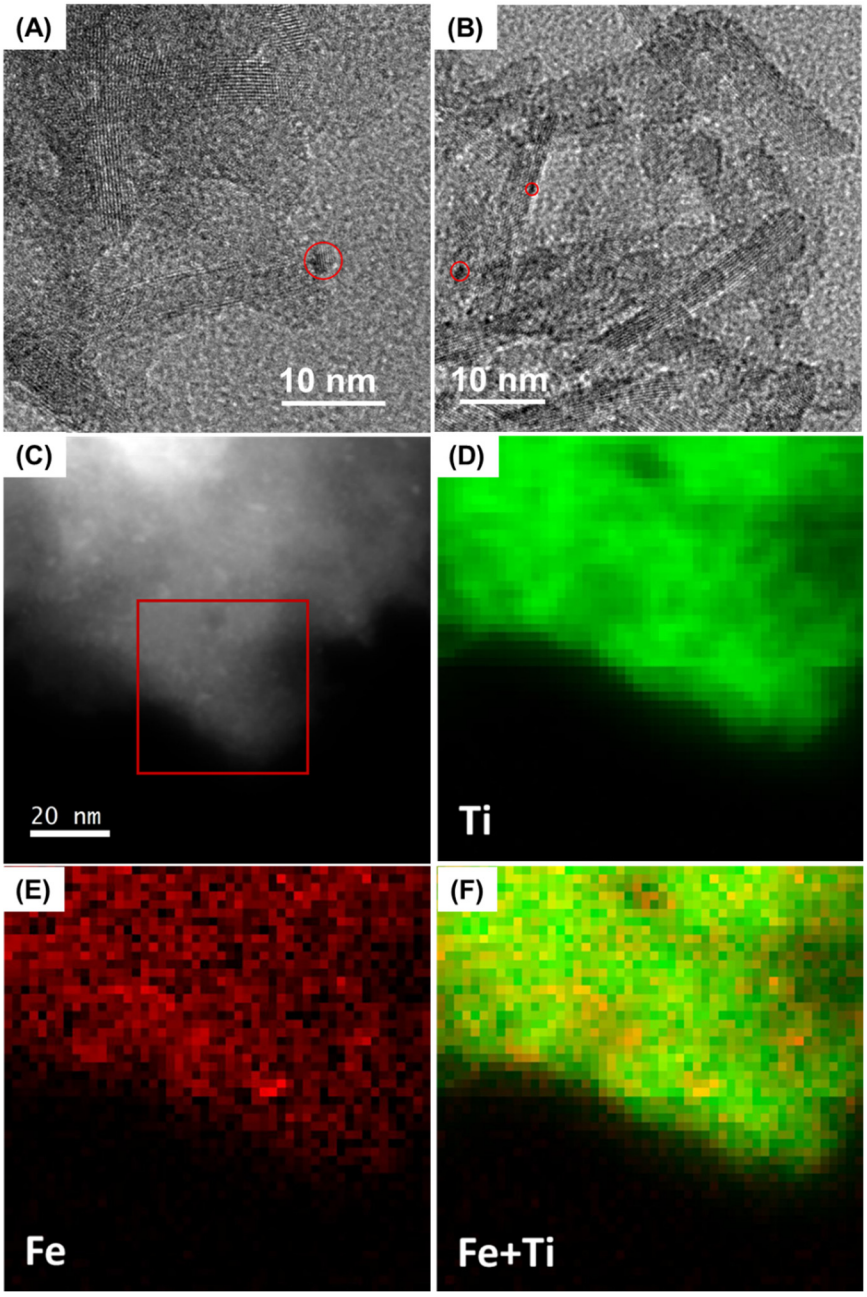

Figure S16. (**A**, **B**) TEM images of (**A**) Fe-TiO_2 NRs after Pt deposition, and (**B**) after 16-hour photocatalysis, with typical Pt NPs deposited on TiO_2 highlighted in red circles; (**C** – **F**) STEM-HAADF image and corresponding HAADF-EELS mapping of spent Fe-TiO_2 NRs after a 16-hour photocatalysis testing.

Table S1. Binding energies and optimal geometries for adsorbates on brookite TiO_2 (001) and (210) with teal, red, grey, white, blue, green illustrate Ti, O, C, H, N, Cl.

	(210)	(001-Auto Reconstructed)
OAm	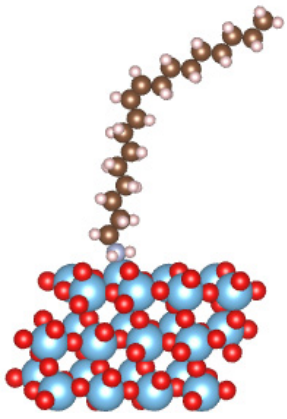 **-0.93 eV**	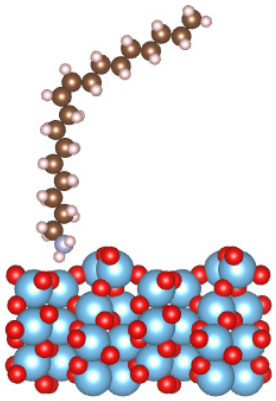 **-0.07 eV**
OAc	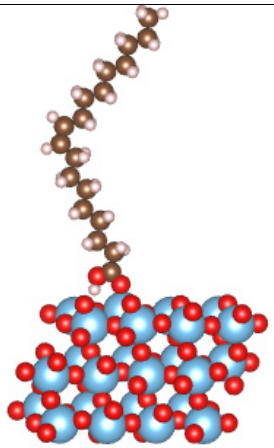 **-0.44 eV**	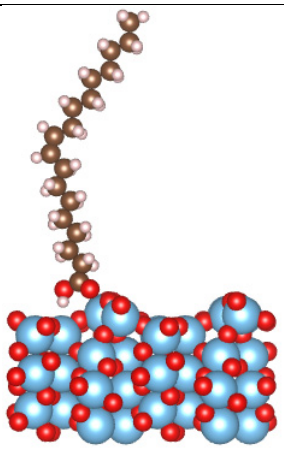 **-0.24 eV**
Cl	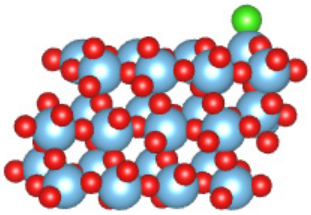 **-0.72 eV**	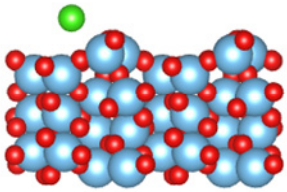 **-0.06 eV**

References:

1. Buonsanti, R.; Grillo, V.; Carlino, E.; Giannini, C.; Kipp, T.; Cingolani, R.; Cozzoli, P. D., Nonhydrolytic Synthesis of High-Quality Anisotropically Shaped Brookite TiO_2 Nanocrystals. *J. Am. Chem. Soc.* **2008,** *130* (33), 11223-33.
2. Cargnello, M.; Montini, T.; Smolin, S. Y.; Priebe, J. B.; Delgado Jaén, J. J.; Doan-Nguyen, V. V. T.; McKay, I. S.; Schwalbe, J. A.; Pohl, M.-M.; Gordon, T. R.; Lu, Y.; Baxter, J. B.; Brückner, A.; Fornasiero, P.; Murray, C. B., Engineering Titania Nanostructure to Tune and Improve its Photocatalytic Activity. *Proc. Natl. Acad. Sci. U.S.A.* **2016,** *113* (15), 3966-3971.
3. Dong, A.; Ye, X.; Chen, J.; Kang, Y.; Gordon, T.; Kikkawa, J. M.; Murray, C. B., A Generalized Ligand-Exchange Strategy Enabling Sequential Surface Functionalization of Colloidal Nanocrystals. *J. Am. Chem. Soc.* **2011,** *133* (4), 998-1006.
4. Pepin, P. A.; Lee, J. D.; Murray, C. B.; Vohs, J. M., Thermal and Photocatalytic Reactions of Methanol and Acetaldehyde on Pt-Modified Brookite TiO_2 Nanorods. *ACS Catal.* **2018,** *8* (12), 11834-11846.
5. Wu, Q.; Xiong, S.; Shen, P.; Zhao, S.; Li, Y.; Su, D.; Orlov, A., Exceptional activity of sub-nm Pt clusters on CdS for photocatalytic hydrogen production: a combined experimental and first-principles study. *Catal. Sci. Technol.* **2015,** *5* (4), 2059-2064.
6. Kresse, G.; Joubert, D., From Ultrasoft Pseudopotentials to the Projector Augmented-Wave Method. *Phys. Rev. B* **1999,** *59* (3), 1758-1775.
7. Blöchl, P. E., Projector Augmented-Wave Method. *Phys. Rev. B* **1994,** *50* (24), 17953-17979.
8. Hammer, B.; Hansen, L. B.; Nørskov, J. K., Improved Adsorption Energetics within Density-Functional Theory Using Revised Perdew-Burke-Ernzerhof Functionals. *Phys. Rev. B* **1999,** *59* (11), 7413-7421.
9. Grimme, S.; Antony, J.; Ehrlich, S.; Krieg, H., A Consistent and Accurate Ab Initio Parametrization of Density Functional Dispersion Correction (DFT-D) for the 94 Elements H-Pu. *J. Chem. Phys* **2010,** *132* (15), 154104.
10. Monkhorst, H. J.; Pack, J. D., Special Points for Brillouin-Zone Integrations. *Phys. Rev. B* **1976,** *13* (12), 5188-5192.
11. Gong, X.-Q.; Selloni, A., First-Principles Study of the Structures and Energetics of Stoichiometric Brookite TiO_2 Surfaces. *Phys. Rev. B* **2007,** *76* (23), 235307.